

Thermal compensation system comissioning for O3 and
a study of the the Pockels effect of an AlGaAs coating

Syracuse University

Daniel Vander-Hyde

March 21, 2022

Abstract

Abstract goes here

Dedication

Declaration

I declare that

Acknowledgements

Contents

1	Introduction	1
2	TCS comissioning for O3	2
2.1	The Mode Matching requirements	2
2.2	aLIGO Thermal Compensation System (TCS)	2
2.2.1	TCS preloading for O3	2
2.2.2	RH input conditioning	3
2.3	Higher order TCS	7
2.3.1	Point absorbers	7
2.3.2	Actuation using a CO ₂ laser and mask	8
3	Electro-optic study of a GaAs/Al_{0.92}Ga_{0.08}As coated sample	9
3.0.1	Brownian Thermal Noise	10
3.0.2	Anisotropic media	13
3.0.3	Crystal systems	15
3.1	Phase modulation of light propogating through a anisotropic crystalline thin film stack	19
3.1.1	Coating parameters	19
3.1.2	Analytical approximation	19
3.1.3	Numerical estimate	20
3.2	Projected DARM coupling	20
3.3	Experiment	20
3.3.1	Design	20
3.3.2	$ E_z $ strength estimate	24
3.3.3	Calibration	28
3.3.4	Noise Floor	28
3.3.5	Drive coupling	30

4	Conclusion	32
5	Appendix	33
5.1	The Equipartition theorem and the Fluctuation dissipation theorem	33
5.2	Crystal classification, point groups, and Bravais lattices	35
5.3	Calibration	36
5.4	Laplace calculator / code	37
5.5	MACOR assembly	37
5.6	FSS LTSpice model	38
	References	38

Chapter 1

Introduction

Chapter 2

TCS comissioning for O3

As shown in Chapter 1, increasing input power directly relates to an interferometer's sensitivity to detecting gravitational waves, one implication of this is the necessity for thermal compensation. As the interferometer increases input power, you directly couple more light into the Fabry-Pérot cavity arms. The input test masses, even with extra low absorption ($\approx 400 \text{ ppb} \pm 150 \text{ ppb}$ [alog ? or point absorber paper](#)) still induce thermo-optic effects with the projected circulating arm power of 200 kW. A symptom of this is mode mismatching throughout the interferometer, a problem that contributes to loss of optical power at the anti-symmetric port which can reduce sensitivity two-fold: loss of power to your readout and reduced efficacy of implementing quantum squeezing.

2.1 The Mode Matching requirements

2.2 aLIGO Thermal Compensation System (TCS)

Mode Matching

- Annular actuation with RH actuators
- Central heating with central CO₂ laser

2.2.1 TCS preloading for O3

Reference to TVO's thesis for preloading settings based on his model [1]

2.2.2 RH input conditioning

Some notes about the analytical calculations of RH (There is a paper on this). 12 hours to sample single TCS setting

Optimizing RH thermo-optic response

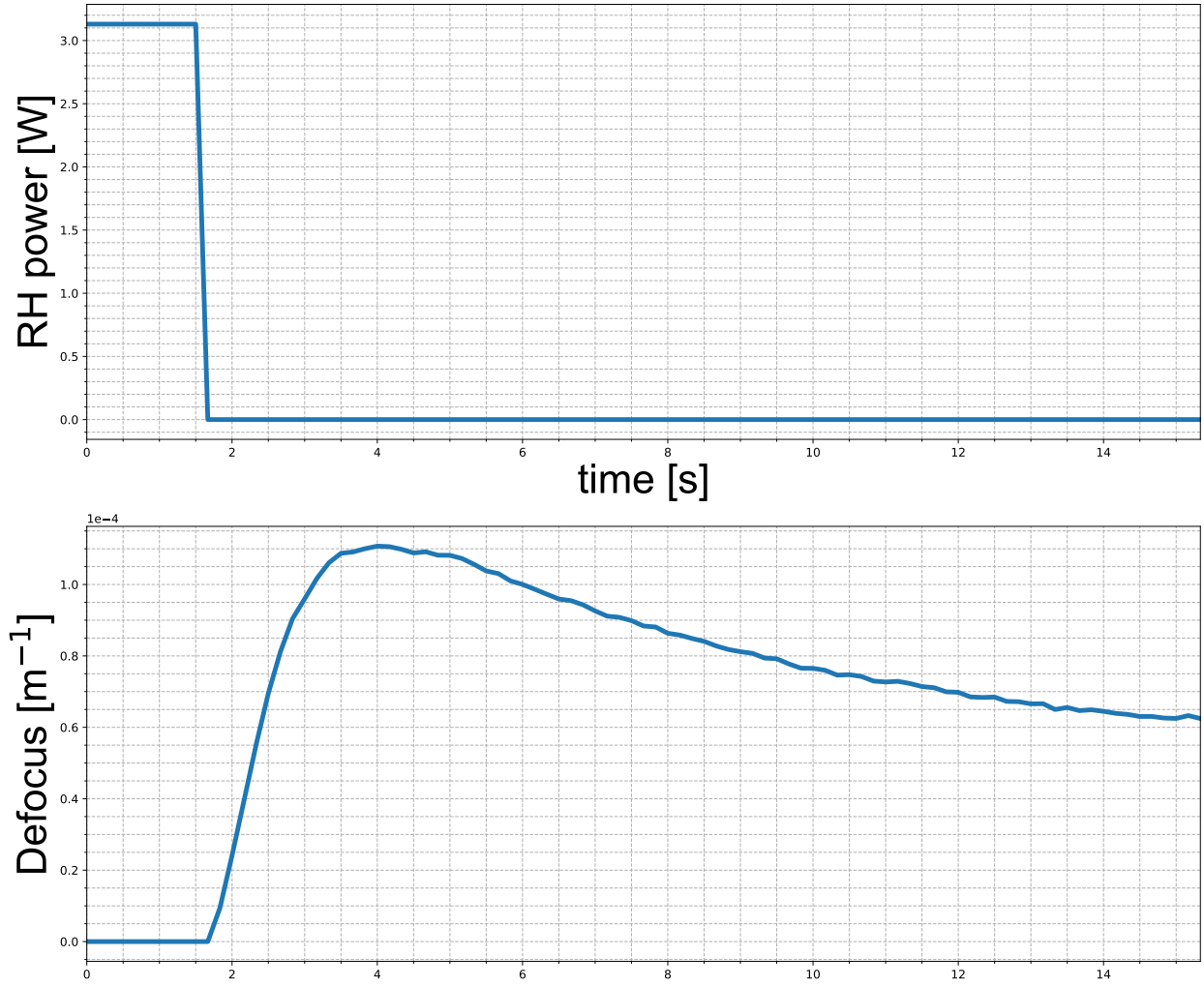


Figure 2.1: ITMY thermo-optic response to a 3.13 Watt power reduction to ring heaters. It's after ≈ 12 hours after the change was made do you start to see a small enough $\frac{d\alpha_{sp}}{dt}$ when you can assume a steady thermal lens.

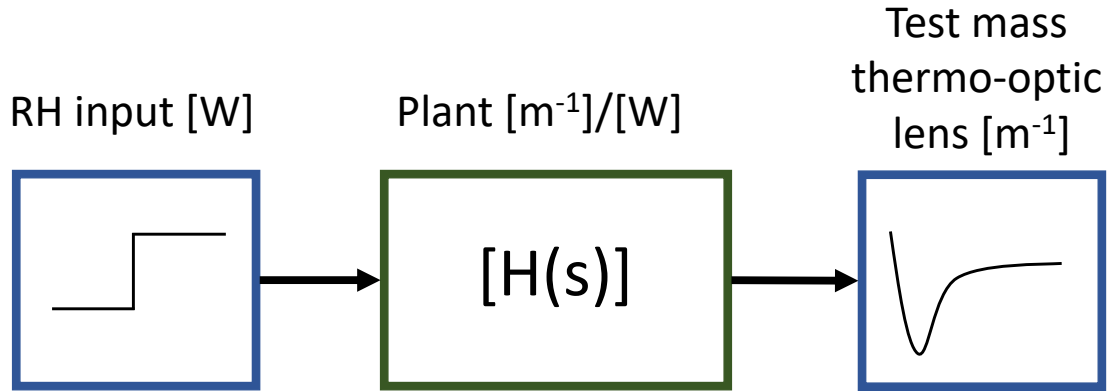


Figure 2.2: A pictograph showing how the plant transforms the signal. The example of this can be seen in Fig [2.1]

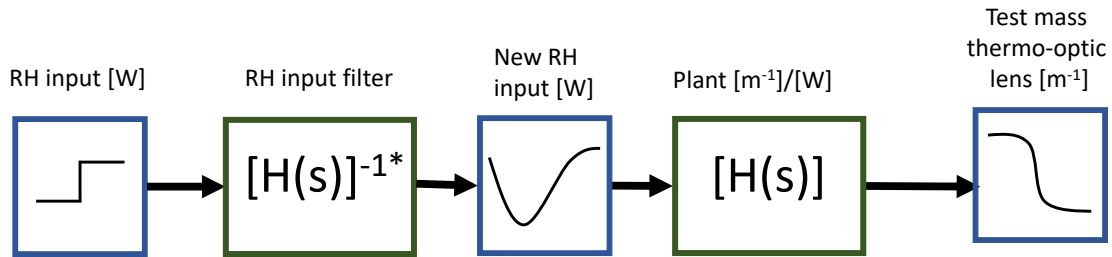


Figure 2.3: A pictograph showing the system with real time digital filtering for an improved thermo-optic response. The RH input filter is created by inverting the plant filter combine with a low pass and added poles to the zpk model to ensure stability.

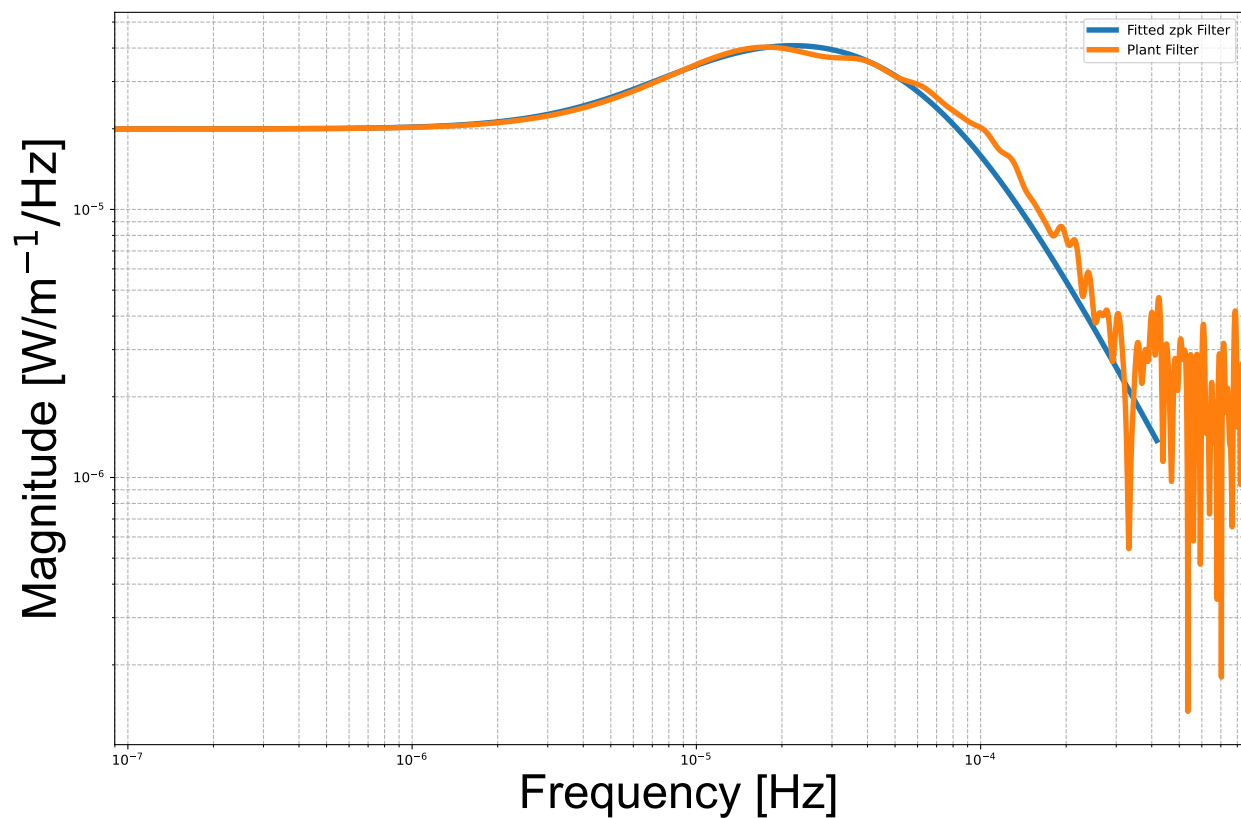


Figure 2.4: Showing the PSD of the RH response (normalized by the input RH power) over a an ≈ 12.5 hour period. The zpk model of the fitted filter ($H(s)$) is $9.2545e - 12 \frac{(s+3.14210e-5)}{(s+8.168e-5)(s+0.0003142)(s+0.0005969)}$

Dynamic Thermal compensation

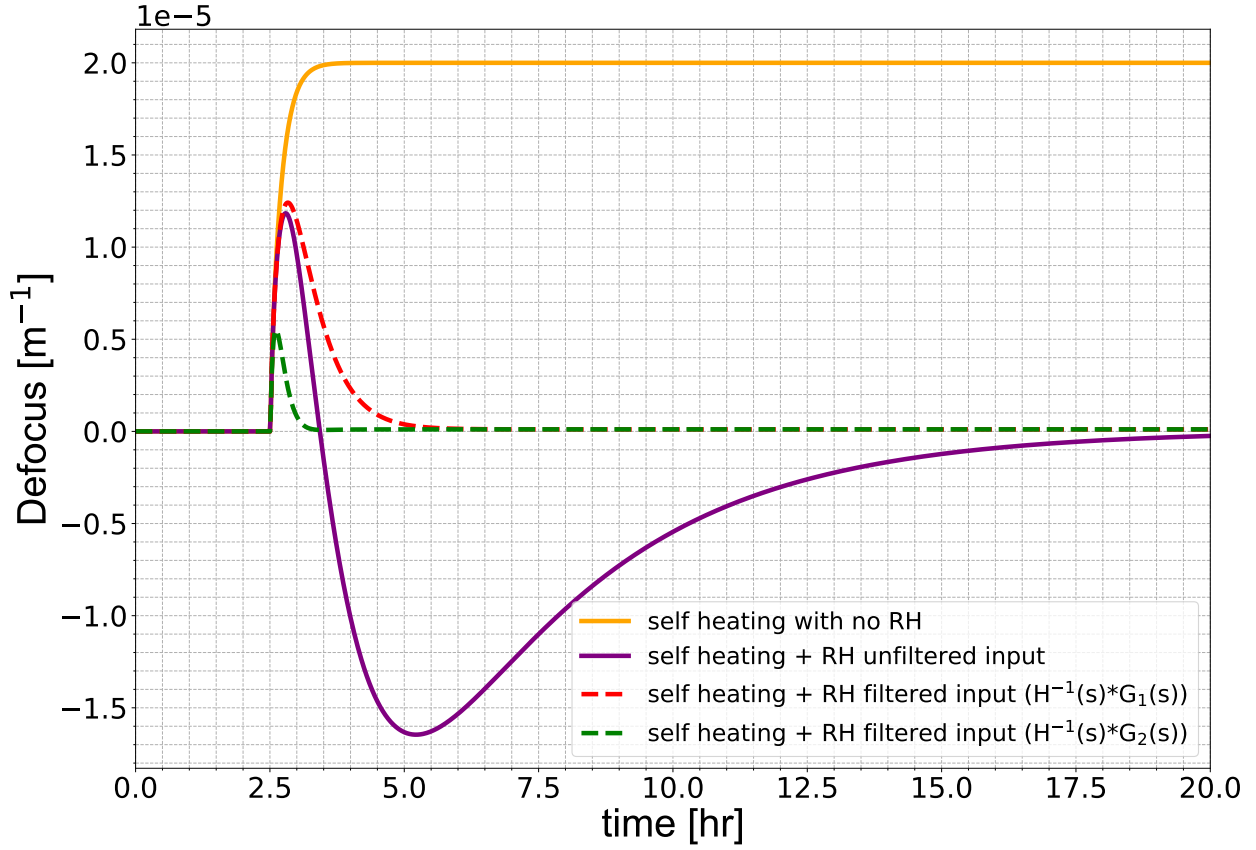


Figure 2.5: Comparison of the natural RH response and the response to the conditioned input. The above plot is simulated in Matlab by passing the RH input time series (top plot) through the $[H(s)]^{-1*}$ and $H(s)$ to acquire with the result lensing behavior on the bottom plot.

Limitations

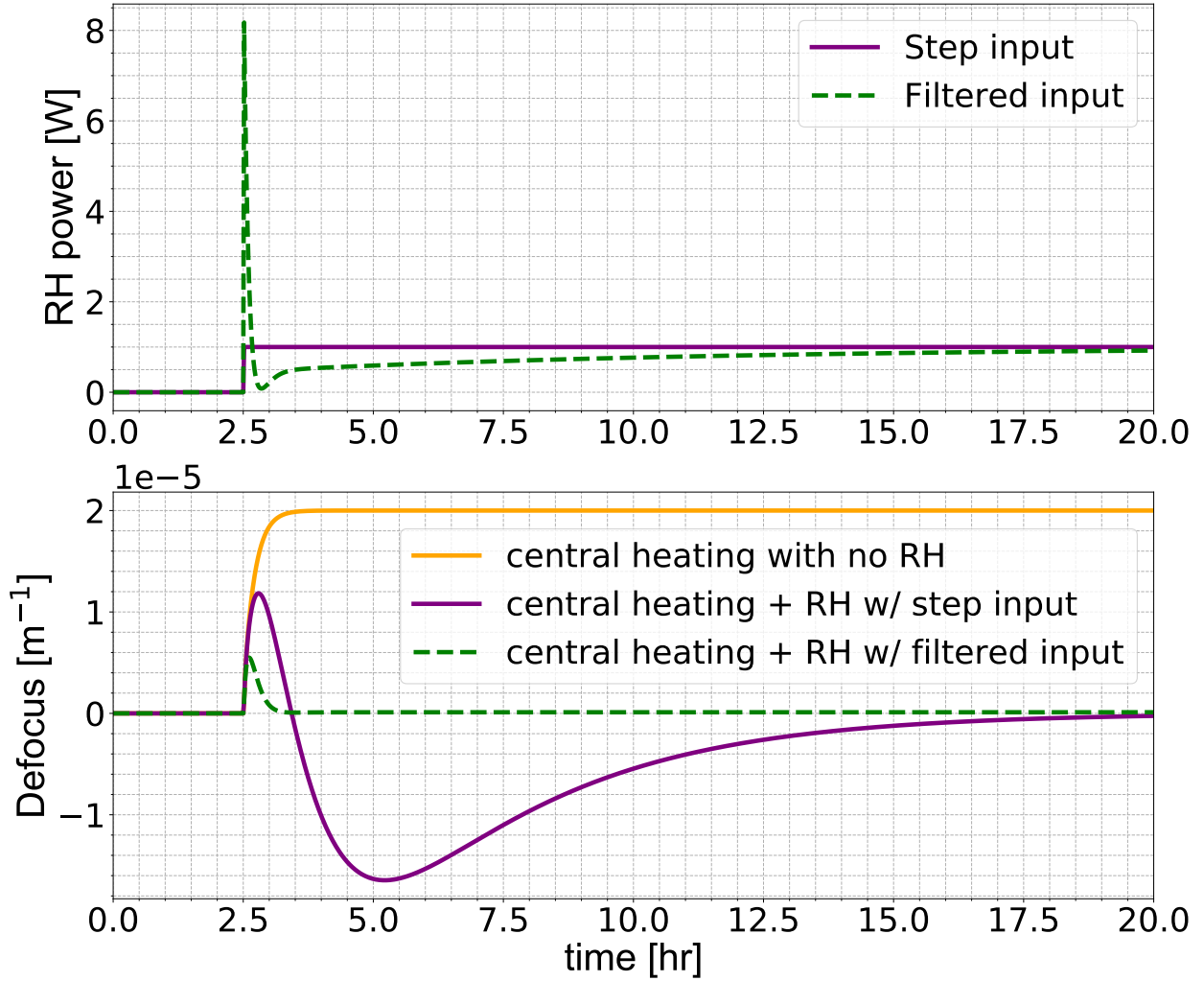


Figure 2.6: Comparison of the natural RH response and the response to the filtered input with RH power

Limitation on RH power is set at 8W Double check source?

Implementation into CDS at LHO

2.3 Higher order TCS

2.3.1 Point absorbers

- Impact on RF sidebands with interferometer thermalization

2.3.2 Actuation using a CO₂ laser and mask

- Aiden's design
- Imaging
- Installation
- Metric of improvement? (Impact on sidebands after thermalization)

Chapter 3

Electro-optic study of a GaAs/Al_{0.92}Ga_{0.08}As coated sample

As mentioned in Section (1?) one of the many LIGO fundamental noise sources is coating thermal noise from the SiO₂/TiO₂ : Ta₂O₅ aLIGO coatings. As aLIGO approaches its designed sensitivity various coating solutions are currently proposed to mitigate thermal noise coupling into the detector output. With the potential to reduce coating Brownian noise by a factor of 10 [2], Al_{0.92}Ga_{0.08}As shows much promise with next generation detectors with a corresponding strain reduction by a factor of (5?) in comparison to the aLIGO coatings, though with different material properties of these crystalline coatings introduce new coating noise couplings.

A notable source of noise is the linear electro-optic property of the crystalline material (dn/dE), also known as the Pockels effect [3]. Characterizing currently proposed Al_{0.92}Ga_{0.08}As coated “witness” samples thorough extensive analysis and experimental data of the aforementioned property is worthwhile for the use of Al_{0.92}Ga_{0.08}As coatings in gravitational wave interferometers. The following section is dedicated to the discussion of brownian thermal noise and the fundamental limit it imposes on gravitational wave detection, the improvements of said limitations with GaAs/Al_{0.92}Ga_{0.08}As coated mirrors over SiO₂/TiO₂ : Ta₂O₅ coatings, the Al_{0.92}Ga_{0.08}As linear electro-optic effect starting with the fundamentals on anisotropic media and the electro-optic tensor of zincblende crystalline materials, estimates of the differential phase of light reflected from a GaAs/Al_{0.92}Ga_{0.08}As coating, and an experiment constructed with the intention of measuring the linear electro-optic effect within a 1kHz \rightarrow 1MHz region.

3.0.1 Brownian Thermal Noise

In 1827 the Scottish botanist Robert Brown noticed a constant motion of pollen particulates on the surface of water; witnessing randomized collisions of the water molecules holding a kinetic energy proportional to the temperature ($k_B T$) [4]. It is because of his documented observations we name the phenomena Brownian motion. And although the observations were on motion of particulates in liquids, molecules and atoms within gases and solids also exhibit Brownian motion. For high precision optical experiments operating at room temperature (and higher due to high power resonant beams), understanding how much differential phase noise is imparted on the interferometer light passing through and reflecting from core optics is crucial. This requires knowledge of the mean squared displacement from each degree of freedom of the system which can be realized through the Fluctuation Dissipation theorem. Derived by H.B. Callen and T.A. Welton, the theorem states that for a randomly fluctuating linear force [5]:

$$F_x^2(f) = 4k_B T \Re[Z] \quad (3.1)$$

Where $\Re[Z]$ is the real part of the impedance of the system. This impedance directly relates to equations of motion:

$$Z = \frac{F}{\dot{x}} \quad (3.2)$$

Another useful form is the power spectrum of the fluctuating motion:

$$x^2(f) = \frac{4k_B T}{(2\pi f)^2} \Re[Y] \quad (3.3)$$

Where Y is the inverse of the impedance or admittance. With this power spectra, modelling and budgeting notable LIGO fundamental noise contributions attributed to the choice of the materials used for mirror substrates, and highly reflective mirror coatings becomes less daunting. Though adequate modelling of internal force couplings for the aforementioned components is required.

Internal friction in Materials and Loss angle

Zener provides a model of the internal friction of materials incorporating anelasticity into the equations of motion [6]:

$$F = k(1 + i\phi)x + m\ddot{x} \quad (3.4)$$

Where m is mass attached to a spring with a spring constant $k(1 + i\phi)$ incorporating the degree of anelasticity ϕ . From equations 3.5 and 3.3 we perform a Laplace transform and acquire the following form of admittance:

$$Y(s) = \frac{\dot{x}(s)}{F(s)} = \frac{-s}{k(1 + i\phi) + ms^2} \quad (3.5)$$

Or more transparently the Fourier representation since we assume a linear time invariant system:

$$Y(\omega) = \frac{\dot{x}(\omega)}{F(\omega)} = \frac{-i\omega}{k(1 + i\phi) - m\omega^2} = \frac{k\omega\phi - i\omega(k - m\omega^2)}{(k - m\omega^2)^2 + k^2\phi^2} \quad (3.6)$$

Plugging equation 3.6 back into 3.3:

$$x^2(f) = \frac{2k_B T}{\pi} \frac{k\phi}{(k - 4\pi^2 m f^2)^2 + k^2\phi^2} \quad (3.7)$$

Computing the admittance from a Gaussian beam impinging upon a HR mirror can require expansion of all individual mechanical degrees of freedom of the test mass system across a relevant frequency range, and with that approach convergence is not guaranteed. Saulson and Gonzalez provide an alternative method to computing the admittance coined the “direct approach” by Levin when computing the noise from a Gaussian beam on a LIGO HR test mass. The admittance can be acquired through:

$$\Re[Y] = \frac{W_{\text{diss}}}{F_o^2} \quad (3.8)$$

W_{diss} is the dissipated power from the system due to an oscillating force F_o . This form of the admittance reveals an important result of the fluctuation dissipation theorem where an undriven system with a dissipative actor, imparts motion to the degrees of freedom via a driving force by virtue of that same actor at finite temperatures. This direct approach also allows the surface pressure applied by the Gaussian beam to interrogate which mechanical modes of the test mass impose a significant energy when 3.8 is plugged into 3.3. In the case of the gaussian beam / uncoated test mass studied by Levin [7]:

$$S_x(f) = \frac{4k_B T}{f} \frac{1 - \sigma^2}{\pi^3 E_o r_o} I\phi \left[1 - O\left(\frac{r_o}{R}\right) \right] \quad (3.9)$$

Refer to Levin appendix for more on how elasticity parameters are introduced? Where ϕ and E_o are the Poisson ratio and Young’s modulus respectively, and $O(\frac{r_o}{R})$ contains a correction term contribution as a function of the small beam radius (r_o) relative to the mirror radius (R).

Coating Brownian thermal noise

Further investigations into the beam/optic system utilizing this approach and elasticity theory led to a deeper understanding about Brownian thermal noise contributions from LIGO test masses (substrate, suspensions, HR coating). Levin mentions, with details from Harry, that the noise contributed by a lossy mirror coating is proven to be the most significant contributor of brownian thermal noise. Hong provides a power spectral density [8]:

$$S_j^X = \frac{4k_B T \lambda \phi_x^j (1 - \sigma_j - 2\sigma_j^2)}{3\pi^2 f Y_j (1 - \sigma_j)^2 \omega_o^2} \quad (3.10)$$

Where X represents bulk and shear with $j = \text{odd}$ (material 1) and $j = \text{even}$ (material 2) alternating layers representing high and low index materials $j = \text{odd}$ (material 1) $j = \text{even}$ (material 2) for an HR coating.

SiO₂/TiO₂ : Ta₂O₅ coating parameters

Currently the LIGO interferometers deposit $\lambda/4$ stacks of silica and titania doped tantala on fused silica test mass substrates. Effective loss angle measurements [9]

Current SiO₂/TiO₂ : Ta₂O₅ elasticity params, power spectra, and strain spectral density (order of magnitude estimate)

GaAs/Al_{0.92}Ga_{0.08}As coating parameters

Specific coating parameters for most promising Al_{0.92}Ga_{0.08}As candidates? Chat with Steve. Or just mention parameters that are listed in Cole 2013 [2]

Insert computed curves of the most precise and recent (effective) loss angle measurements (Nick Demos measurements?). More instructive to plot strain spectral density or displacement power spectra

Currently thermal noise from the SiO₂/TiO₂ : Ta₂O₅ optical coatings is the largest contributor of Brownian noise in LIGO compared to estimated substrate and suspension thermal noise [9]. As of the end of O3, Brownian thermal noise is estimated to be ? orders of magnitude below the current sensitivity and it will prove to be the limiting source of noise as that sensitivity is increased with various other upgrades mitigating fundamental and technical noise. (already mentioned in intro prior to this thermal noise section. Need to re-iterate in more detail?)

3.0.2 Anisotropic media

Unlike with isotropic media, we cannot assume that the index of refraction of anisotropic media is the same for all chosen wave vectors. This is a direct consequence of the birefringence of anisotropic media; characterized by the dielectric, permittivity, and polrization tensors.

The Dielectric tensor

Further elaborating on the nature of a generalized dielectric tensor for any wavevector is required to proceed:

$$D_i = \varepsilon_{ij}E_j \quad (3.11)$$

Where D is the displacement vector and E is the electric field vector and ε is the dielectric tensor. The displacement vector for isotropic media is retrieved when $i = j$ and $\varepsilon_i = \varepsilon$. To further understand the nature of the dielectric tensor we assert Poynting's theorem providing an energy conservation requirement:

$$\nabla \cdot \vec{S} = \frac{dU}{dt} \quad (3.12)$$

Where $\vec{S} = \vec{E} \times \vec{H}$ is the poynting vector and $U = \frac{1}{8\pi}(\vec{E} \cdot \vec{D} + \vec{B} \cdot \vec{H})$ is the electromagnetic field density. The reader is left to perform the exercise and show that in order for 3.12 to hold true given 3.11

$$\varepsilon_{ij} = \varepsilon_{ji} \quad (3.13)$$

Stating that the dielectric tensor holds only six unique terms. The energy density is represented as an ellipsoid but with a coordinate transformation we can diagonalize and realize principal axes of the dielectric allowing a simpler form of the displacement, and in turn the energy density.

Monochromatic plane wave propogation

Revisiting Maxwell's equations for simple monochromatic plane wave solution gives provides further direction on how crystalline media may effect impinging light. Further elaborating, the following assumptions are made:

$$\vec{E} = E_o e^{(i\omega(\frac{n}{c}\vec{r} \cdot \vec{s} - t))} \quad (3.14)$$

Where n is the index of refraction, c is the speed of light, \vec{r} is the position vector and \vec{s} is the unit wave normal.

$$\nabla \times \vec{H} = \frac{\partial \vec{D}}{\partial t} \quad (3.15)$$

Where \vec{H} is the magnetic field assuming the permeability μ , and the generalized displacement vector \vec{D} and electric field vector \vec{E} .

$$\nabla \times \vec{E} = -\mu \vec{H} \quad (3.16)$$

Reducing to only the displacement and electric fields:

$$\vec{D} = \frac{n^2}{\mu} [\vec{E} - \vec{s}(\vec{s} \cdot \vec{E})] \quad (3.17)$$

Maxwell's equations show that the electric field is not necessarily parallel to the displacement field and in most materials with non-zero polarizability tensors and dielectric tensors, it is not. But as specified above, the displacement vector, Electric field and unit wave normal are co-planar while remaining orthogonal to \vec{H} . Assuming we are operating within a coordinate system aligned with the principal dielectric axes, we substitute 3.11 into 3.17:

$$E_i = \frac{n^2 s_i (\vec{E} \cdot \vec{s})}{n^2 - \mu \varepsilon_i} \quad (3.18)$$

From here it can be shown that for a general plane wave there exist two unique refractive index solutions within the constructed dielectric. Though using this result to show this requires revisiting geometrical conditions that are best visualized using a method introduced in the next section. **For a more rigorous proof, see Appendix H in [10]**

Indicatrix

Acquiring solutions of the two indices along with the corresponding directions of propagation in the crystal for a general plane wave with unit wave vector \vec{s} can be done via a convenient geometrical construction. The construction begins by considering a constant electric energy density (U_e) surface in the \vec{D} space; an ellipsoid is formed:

$$\frac{D_x}{\varepsilon_x} + \frac{D_y}{\varepsilon_y} + \frac{D_z}{\varepsilon_z} = 2U_e \varepsilon_o \quad (3.19)$$

With redefined coordinates $(\vec{D}/\sqrt{2U_e \varepsilon_o}) \rightarrow \vec{r}$ and setting $\varepsilon_i = n_i^2$:

$$\frac{x^2}{\varepsilon_x} + \frac{y^2}{\varepsilon_y} + \frac{z^2}{\varepsilon_z} = 1 \quad (3.20)$$

This equation for the ellipsoid is known as the indicatrix. Given the co-planar solution demonstrated in the last section, we can impose the normal of the plane $\vec{r} \cdot \vec{s} = 0$:

$$\vec{r} \cdot \vec{s} = xs_x + ys_y + zs_z = 0 \quad (3.21)$$

Equations 3.19 and 3.21 both contribute constraints to the method of finding extrema using Lagrange multipliers for the function:

$$r^2 = x^2 + y^2 + z^2 \quad (3.22)$$

The Lagrangian (\mathcal{L}) with the introduced multipliers (λ_1, λ_2) then becomes:

$$\mathcal{L}(\vec{r}, \vec{s}, \lambda_1, \lambda_2) = x^2 + y^2 + z^2 + \lambda_1(xs_x + ys_y + zs_z) + \lambda_2\left(\frac{x^2}{\varepsilon_x} + \frac{y^2}{\varepsilon_y} + \frac{z^2}{\varepsilon_z} - 1\right) \quad (3.23)$$

With the generated system of equations from the Lagrange multiplier method ($\partial F_i / \partial x_i = 0$, and $\partial F_j / \partial \lambda_j$) where index $i = x, y, z$ and $j = 1, 2$ we obtain a system of 3 equations:

$$i\left(1 - \frac{r^2}{\varepsilon_i}\right) + s_i\left(\frac{xs_x}{\varepsilon_x} + \frac{ys_y}{\varepsilon_y} + \frac{zs_z}{\varepsilon_z}\right) = 0 \quad (3.24)$$

The result is verified when substituting $r \rightarrow \frac{\vec{D}}{\sqrt{\vec{E} \cdot \vec{D}_{\varepsilon_o}}}$ back which recovers 3.18.

Figure here would be nice

3.0.3 Crystal systems

The following section is intended to provide an adequate crystallographic background to allow the further the discussion of light propagation through GaAs and Al_{0.92}Ga_{0.08}As. This includes, crystal classification, the optical crystal classification of GaAs and Al_{0.92}Ga_{0.08}As under “normal” operating conditions, and optical crystal classification of GaAs and Al_{0.92}Ga_{0.08}As with electrical and mechanical perturbations.

Crystal classification

The priority of this section is to provide a crystallographic background to some conventions behind the classification and characterization of crystalline materials through the usage of: Miller indices, unit cells, point groups, Bravais lattices and space groups.

The fundamentals of crystal categorization come with the emergence of a formal study of crystals (crystallography) in the 17th and 18th centuries through the macroscopic analysis of planar fractures of crystals (cleavage planes). Nicolaus Steno and René-Just Haüy are credited with the discovery of the three crystallographic laws: law of constant interfacial angles (Steno), the law of rational indices (Haüy), and the law of constancy of symmetry (Haüy) [11].

The **law of constant interfacial angles** states that the angles between two adjacent faces of a crystal species is a constant [?].

The **law of rational indices** states that the intersection of the three intercepts of a crystal plane with the crystallographic axes are constant and can be expressed by rational numbers and whole number multiples of them. Alongside this law Haüy would go on to hypothesize that crystals are composed of polyhedral molecules arranged in a periodic manner in three-dimensional space [?]. This early geometric model of crystals, provided fundamental tools of crystallography that we still use today. The modern unit cell is represented by the smallest geometric atomic/molecular arrangement that represents the symmetry of the crystal. When representing a more macroscopic form of the crystal these unit cells are assembled periodically in 3d space along a grid of points known as a lattice[12].

The **law of constancy of symmetry** states that crystals of a particular substance maintain the same symmetry elements [?]. This discovery garnered interest in the 19th century to classify crystal structures under the framework of symmetry groups **more on groups in appendix**. Point group symmetries were first addressed and sorted crystals into 32 crystallographic point groups. Soon after translational symmetries were addressed by Auguste Bravais with 14 different lattice structures which also implicitly displayed a formal connection between unit cell geometry and lattice structures [11]. The combination of these point group symmetries and translational symmetries addressed by the Bravais, form a new group known as the crystallographic group: a subset of the more generally space group **for more details on point groups, Bravais lattices and space groups, see appendix**.

GaAs and Al_{0.92}Ga_{0.08}As classifications

The space group of GaAs as well as Al_{0.92}Ga_{0.08}As are within the $F\bar{4}3m$ space group. Crystals with this particular space group are commonly known as zincblende crystals; a common

crystal configuration named after zinc sulfide (ZnS). Cubic crystals by their crystallographic structure display optically isotropic characteristics when no DC and/or slowly varying electric fields are present and are not mechanically perturbed.

Insert figure of GaAs structure (Shapr3D construction)

Mention the difference in lattice cell constant between GaAs and Al_{0.92}Ga_{0.08}As

Perturbed GaAs and Al_{0.92}Ga_{0.08}As

AlGaAs is a cubic crystal, optically isotropic BUT birefringence can be induced (displays characteristics of an uniaxial crystal)

Is this true? Satoshi, I believe so. There seem to be some geometric differences between GaAs and Al_{0.92}Ga_{0.08}As in terms of Bravais lattices but Adachi claims it's essentially zincblende. To verify it's important to know how the change in the Bravais lattice might change the unit cell and if it's relevant. Otherwise the birefringence we have seen upon installation was stress induced.

There seems to be different accounts of a measured birefringence from HR GaAs / Al_{0.92}Ga_{0.08}As (Satoshi, CTN, Aidan)

Is the measured birefringence static? (Layer bonding method might introduce something?)

Does it change from different mounting methods? (Photoelastic)

Electro-optic could probably be ruled out based on ambient field measurements.

Measurement precision of the coating birefringence? Cavity length, Polarization drifts, etc.

The pockels effect

Some anisotropic crystalline media (ACM) exhibit characteristics where the indicatrix changes as a function of a slowly (is this statement correct?) I can very much word this better. Right now it probably is not correct. (up to the speed of sound within the media?) varying electric field [13, 10].

Indicatrix with electro-optic coefficients

Relationship between a slowly varying electric field vector of an arbitrary direction $\vec{E} =$

$[E_1, E_2, E_3]$ to the perturbations of the indicatrix:

$$\begin{bmatrix} \left(\frac{1}{\Delta n^2}\right)_1 \\ \left(\frac{1}{\Delta n^2}\right)_2 \\ \left(\frac{1}{\Delta n^2}\right)_3 \\ \left(\frac{1}{\Delta n^2}\right)_4 \\ \left(\frac{1}{\Delta n^2}\right)_5 \\ \left(\frac{1}{\Delta n^2}\right)_6 \end{bmatrix} = \begin{bmatrix} r_{11} & r_{12} & r_{13} \\ r_{21} & r_{22} & r_{23} \\ r_{31} & r_{32} & r_{33} \\ r_{41} & r_{42} & r_{43} \\ r_{51} & r_{52} & r_{53} \\ r_{61} & r_{62} & r_{63} \end{bmatrix} \begin{bmatrix} E_1 \\ E_2 \\ E_3 \end{bmatrix} \quad (3.25)$$

The six indices correspond to the six unique elements in the indicatrix.

Nye (Chapter 8.2)

Yariv (Chapter 14)

How the modulation of the phase of the carrier field is dependent on the orientation of its wave vector with respect to the crystal structure, the modulating electric field direction and strength, (other items to discuss in terms of introducing the effect)

This property of ACM is what allows electro-optic modulators to operate as light phase modulators

Electro-optic tensor for zincblende structures with $\bar{4}3m$ point group symmetry

$$\begin{bmatrix} 0 & 0 & 0 \\ 0 & 0 & 0 \\ 0 & 0 & 0 \\ r_{41} & 0 & 0 \\ 0 & r_{41} & 0 \\ 0 & 0 & r_{41} \end{bmatrix} \quad (3.26)$$

$$r_{41} = r_{52} = r_{63}$$

For GaAs @ 10.6 μ $r_{41} = 1.6 \times 10^{-12}$ [m/V]

Adachi estimate for Al_xGa_{1-x}As?

Specific propogation (Which Miller index?) direction of 1064 nm light through GaAs and AlGaAs

3.1 Phase modulation of light propogating through a anisotropic crystalline thin film stack

3.1.1 Coating parameters

Is the sample that we have a standard AlGaAs sample from Thorlabs/CMS?

Growth orientation (Miller indices) with respect to substrate surface

- Mirror surface is the [100] plane.
- Within the [100] plane the AlGaAs coating is grown with a flat indicator that draws a line within the [0-11] plane where the surface normal is pointing towards the sample center.

Layering

The coating to be studied consists 36 $\lambda/4$ thick layers of GaAs interspersed with 35 layers of $\lambda/4$ thick AlGaAs. GaAs forms the top and bottom layer to protect the AlGaAs from absorbing oxygen from the air. High Index: GaAs, $n=3.480$, layer thickness is 76.43 nm Low Index: Al_{0.92}Ga_{0.08}As, $n=2.977$, layer thickness is 89.35 nm [Info from Steve. Written source?](#)

3.1.2 Analytical approximation

Fejer and Bonilla take an analytical approximation approach when finding the impact of the electric field to the change in phase of the light through a crystalline anisotropic thin film ($\lambda/4$) stack [14].

$$\hat{\phi}' = \frac{\pi n_1 z}{1 - z^2} (z^{2N} - 1) \frac{z^{2N} \frac{(n_f)^2}{n_2 n_3} (n_2 \kappa_{\gamma 2} + n_3 \kappa_{\gamma 3}) - (n_2 \kappa_{\gamma 3} + n_3 \kappa_{\gamma 2})}{(n_1)^2 - (n_f)^2 z^{4N}} \quad (3.27)$$

with $z = \frac{n_2}{n_3}$ and $\kappa_{\gamma j} = \frac{d}{d\gamma} \log(n_j h_j) |_{\gamma=\gamma_0} \left(\frac{\hat{n}'_j}{\hat{n}_j} + \frac{\hat{h}'_j}{\hat{h}_j} \right)$

With κ being a scalar parameter.

[Adding a schematic would be helpful.](#)

[Figure is in the works](#)

3.1.3 Numerical estimate

In the appendix of [15] Ballmer explains a formalism that allows the coating transfer function given a differential change in phase due to a scalar parameter to be expressed as follows:

$$M = Q_N D_N \dots Q_k D_k \dots Q_1 D_1 Q_0 \quad (3.28)$$

For a single pass through the coating where the coating thickness and indices are left general.

Both approaches are essentially based on the same calculation method i.e., transfer matrices.

3.2 Projected DARM coupling

To estimate how much DARM coupling can occur, we use use a measured field spectra acquired from installed electric field meters located within LIGO Hanford Observatory EX and EY vacuum chambers. Taking the upper and the lower EFM measurements in .3 [V/m/ $\sqrt{\text{Hz}}$] @ 60 Hz and 4×10^{-3} [V/m/ $\sqrt{\text{Hz}}$] @ 4kHz [16]. I don't think these values are calibrated. According to Martynov et al. 2016, the fluctuations in the electric filed is $\sim 10^{-5}$ [(V/m)/ $\sqrt{\text{Hz}}$]. This along with computed estimate above allows us to create an upper limit for what this noise might be assuming incoherent fields between the end stations and a flat frequency response within LIGO's bandwidth.

3.3 Experiment

To probe for this effect, we took the approach of an in-air Fabry-Pérot cavity with a GaAs/Al_{0.92}Ga_{0.08}As coated sample end mirror mounted in a custom designed MACOR mount with the ability to install electrodes maintaining a fixed distance from the sample surfaces for a controlled E-field injection. Details and specifications are discussed as well as relevant measurements. An improved experimental design is also detailed for a higher sensitivity measurement.

3.3.1 Design

This section details the Pound-Drever-Hall servo which is at the heart of this experiment, the on-table design, a sample / electrode assembly used for a controlled electric field injection, and electrode drive parameters

PDH servo

The Pound-Drever-Hall technique, originally imagined for laser frequency stabilization to an ultra-stable length reference, achieves constant resonance with said reference by tracking the phase of the cavity input light with respect to the light reflected from the cavity. Tracking the approximately linear phase response across resonance is at the heart of this technique and recognizes that physical property to be probed around a cavity's resonance cannot be the intensity of the transmitted or reflected light because of the quadratic symmetry. (Derivative of the intensity could work but depends on us operating off resonance)

Insert figure of reflected intensity and phase response around resonance (cavity transfer function). Maybe also have a figure corresponding to what this could represent in a lab. (sweeping a mirror of the laser cavity through resonance)

Another novelty and insight to the technique is the use of phase modulation onto the carrier field which is the mathematical and physical equivalent to imposing separate optical fields which in most cases do not resonate in the optical cavity.

$$E_{\text{inp}} = E_o e^{i\omega t + \beta \sin(\Omega t)} \quad (3.29)$$

Approximation with Bessel functions (assumptions about modulation depth)

$$E_{\text{inp}} \approx E_o E_0 [J_0(\beta) e^{i\omega t} + J_1(\beta) e^{i(\omega+\Omega)t} - J_1(\beta) e^{i(\omega-\Omega)t}] \quad (3.30)$$

Discuss how the measurement of the beat power between the sideband and the carrier at the RFPD tracks the phase and how with demodulation and filtering, you can create an error signal.

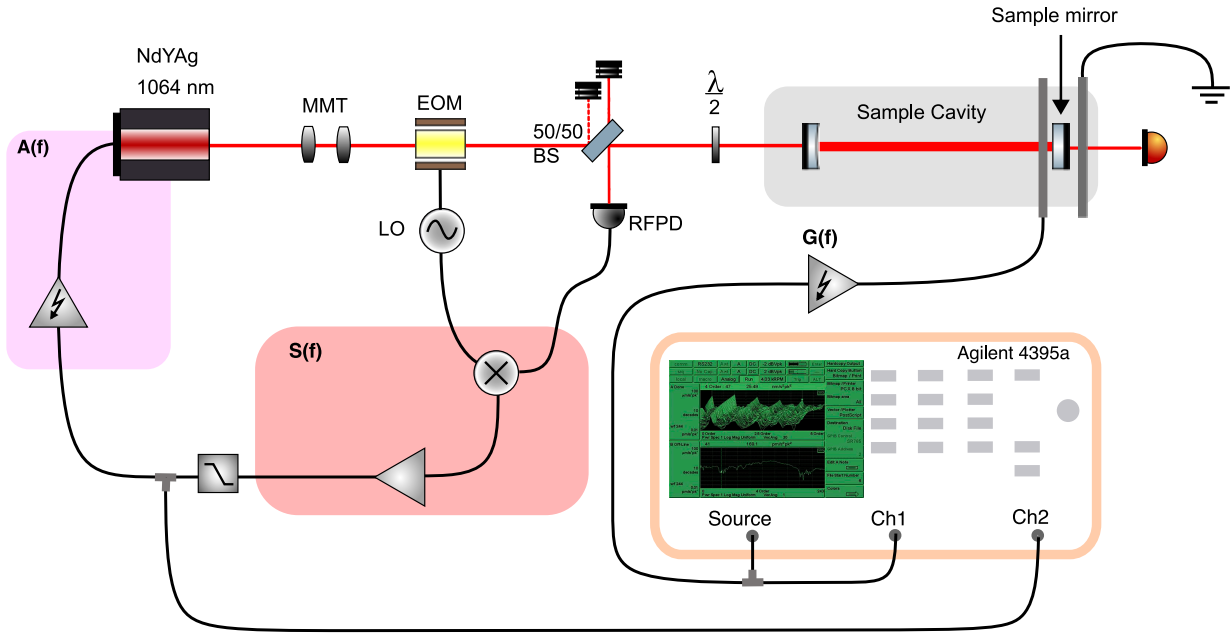


Figure 3.1: Simplified experiment schematic

On-table schema

A figure that highlights path that is intended for locking onto the PMC, and a different color highlight for the path to the experiment

The setup presented in this section, branches off of a previously established optical path used to lock onto a separate optical cavity (PMC).

The laser light source is a Mephisto 2000 NE 1064nm laser.

25 MHz EOM is a New Focus Model 4003 IR resonant phase modulator.

The designed cavity is a 0.1651 m long cavity with a HR IBS coated sample (PL-CC, ROC = 0.333 m) input coupler from CVI Melles-Griot and a GaAs/Al_{0.92}Ga_{0.08}As (PL-PL) fused silica substrate by the Crystalline Mirror Solutions (CMS) division of Thorlabs with the aforementioned parameters (mentioned in coating parameters section).

Sensing S(f)

- 25 MHz RFPD
 - Transimpedance measurement (necessary? or should I just use the mixer out PDH to summarize PD/mixer response)
- Frequency Stabilization servo (modified MIT FSS (DCCD980536)) (LTspice model in appendix)

Actuation A(f)

- Mephisto 2220 PZT response (capacitance estimated from HVA drive measurement with and without connection to PZT)
- Channel 3 of SVR 350-3 BIP High Voltage Amplifier from Piezomechanik GmbH with Pomona box (elog 412)
- **Figure of frequency response of A(f)**

Low frequency servo (Thermal loop)

- Passed signal from FSS → integrators → Laser thermal actuator input

OLG(f)

Isn't quite $A(f) * S(f)$ as stated. Doesn't entirely account for the optical plant. How the measurement is taken (important to take between installations to account for the changes in the optical plant) (elog 831)

Sample / Electrode assembly

Maximizing the electric field ($|E_z|$) and within the coating while requiring a through beam to and through the HR coating lead us to imagine disk electrodes with a 3mm central aperture. The aperture size was chosen to be at least 5 times larger than the beam size at the plate locations. This was to avoid any beam clipping while still allowing to maximize the field strength at the region of interest.

Most commercial optical mounts are conductive which proved to be a problem when attempting to find a mounting solution while reducing the non-normal field gradients within the volume of interest around the sample. Because of this, we chose to construct an optical mount made of MACOR a machinable ceramic with high a high Young's modulus (66.9 GPa), and a moderate Poisson ratio (.29) [17]. An optical mount for the sample made with MACOR, along with glass bearings $.48 \pm .01$ cm \varnothing and a McMaster-Carr 8-32, 1/2" ceramic screw were used to clamp and suspend the optical sample. A 1.24" \varnothing hole was bored into the MACOR with a (**depth?**) depth so that there is a ? mm clearance between the front and back surface of the sample to the electrode plates. **Figure with the sample in-situ**

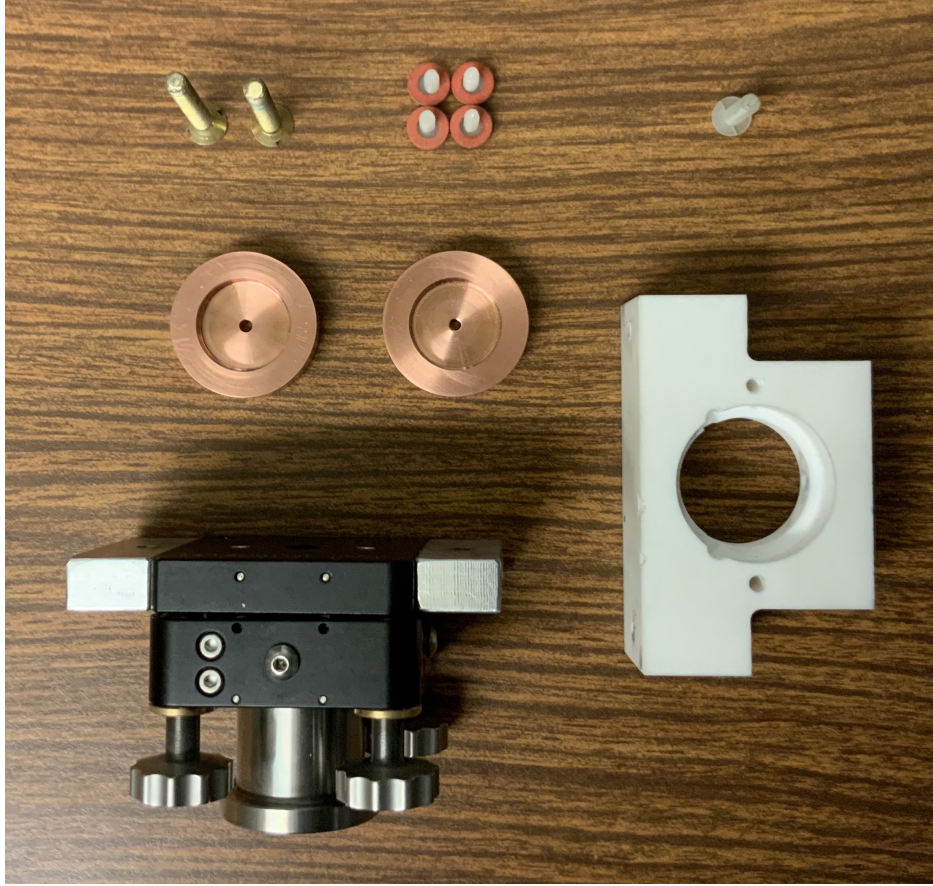


Figure 3.2: Placeholder for more updated MACOR assembly

There are two relevant configurations of this experiment: 1) an all-in-one MACOR assembly where the electrodes are mechanically coupled to the optical mount, and 2) larger mechanically decoupled electrode plates.

A lot of time was dedicated towards preliminary mounts made of PLA and PETG. Do I want to do updated measurements and make statements about noise produced from these mounts?

3.3.2 $|E_z|$ strength estimate

To convey the problem at hand, it is useful to review the illustration seen [here](#) (figure showing the the electrode plates, and sample with AlGaAs coating

Math

To find the Electric field screened by the coating we begin with Gauss' Law:

$$\nabla \cdot D = \rho_{\text{free}} \quad (3.31)$$

For our problem we assume no free charge, but the fused silica substrate with the AlGaAs coating presents dielectric material between the plates. Our initial boundary conditions are also expressed in terms of plate potentials so it is natural to first solve for the potential (V) for every point within our system. We can exploit the cylindrical symmetry with the optic and plate geometry in the r coordinate so we shall express the Laplacian accordingly:

$$(1 - \chi) \left[\frac{1}{r} \frac{\partial}{\partial r} \left(r \frac{\partial}{\partial r} \right) + \frac{\partial^2}{\partial z^2} \right] V = 0 \quad (3.32)$$

Where χ is a spatially dependent electric susceptibility. (Establish coordinates for GaAs/Al_{0.92}Ga_{0.08}As, as well as the fused silica substrate so the computation is transparent)

Definition of ρ must be explained. ρ and ρ_{free} are confusing. Define χ and V .

I will change ρ to r am going to modify figure text so it matches soon.

Utilizing this, we can proceed to a construction of a numerical Laplacian.

Numerical approximation

- Potential map computation in cylindrical
- Computing E_z from potential map
 - inside coating
 - outside coating

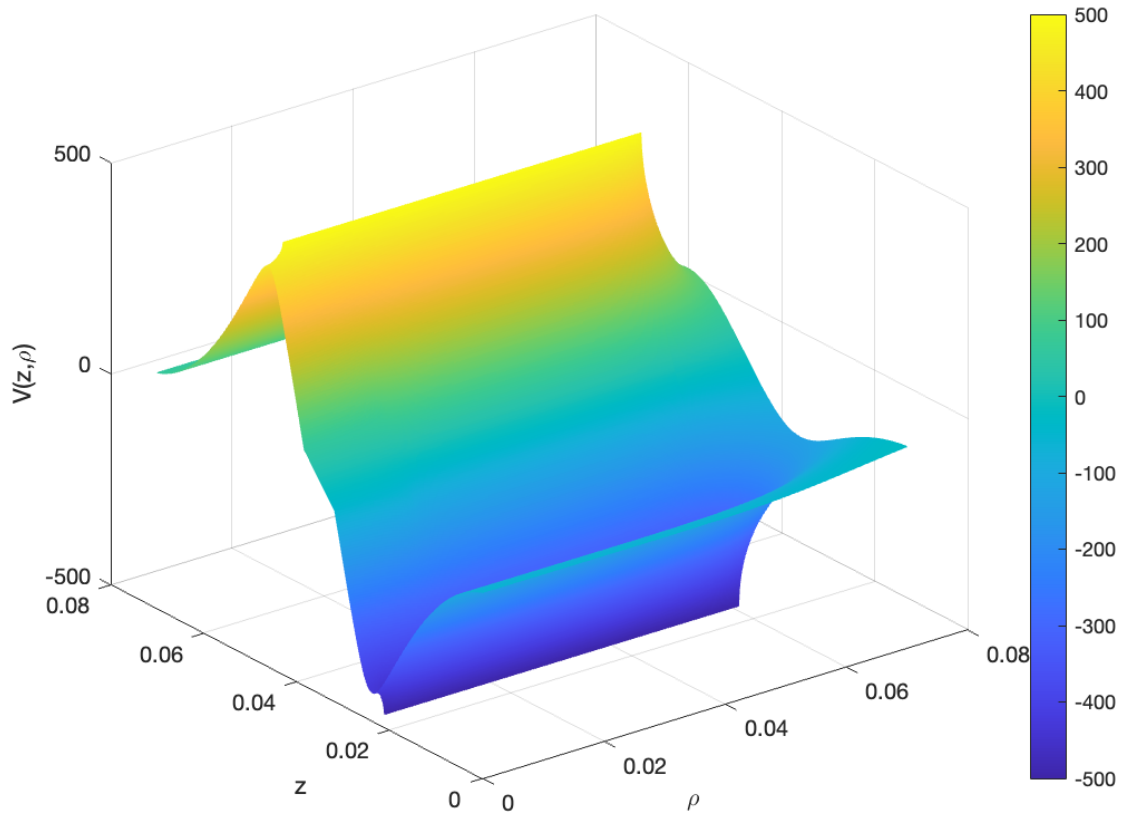


Figure 3.3: Poisson calculator output potential map ($V(z, r)$ in cylindrical coordinates)

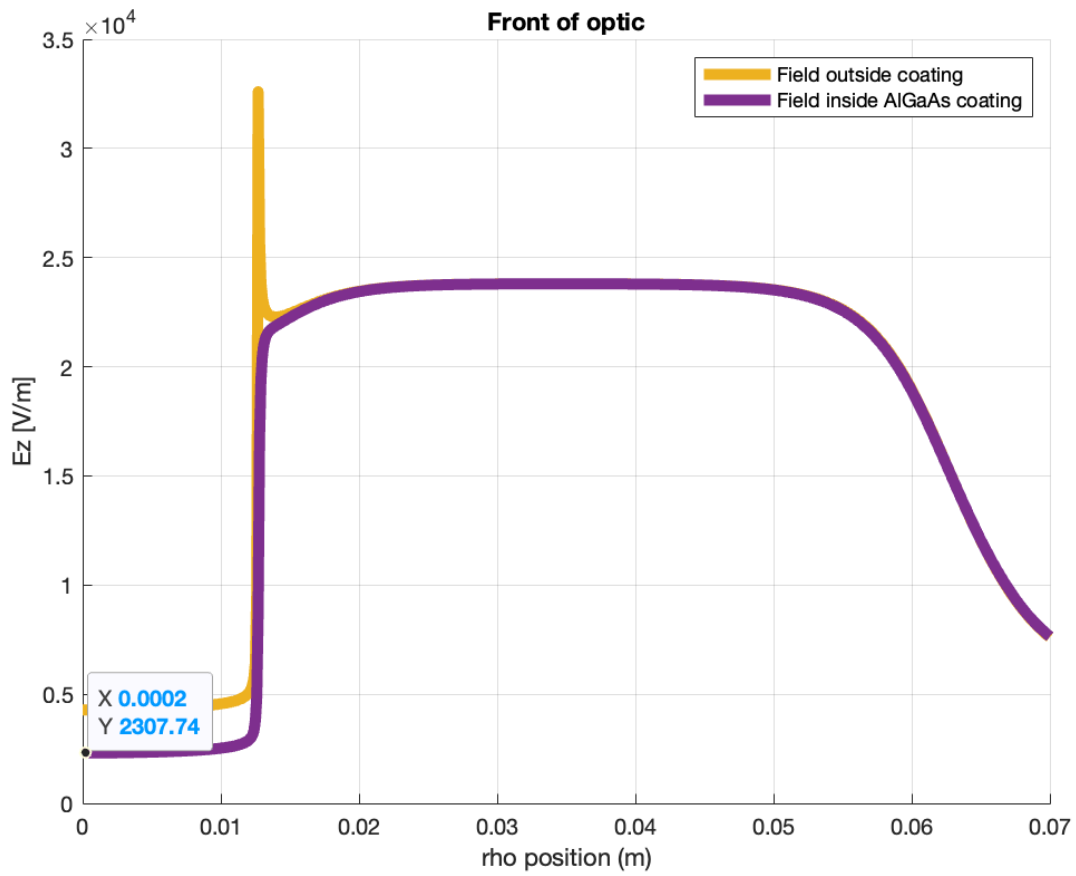


Figure 3.4: $|E_z|$ screened by the coating and immediately outside AlGaAs coating. Needs to be updated with more current settings
How large applied voltage is assumed?

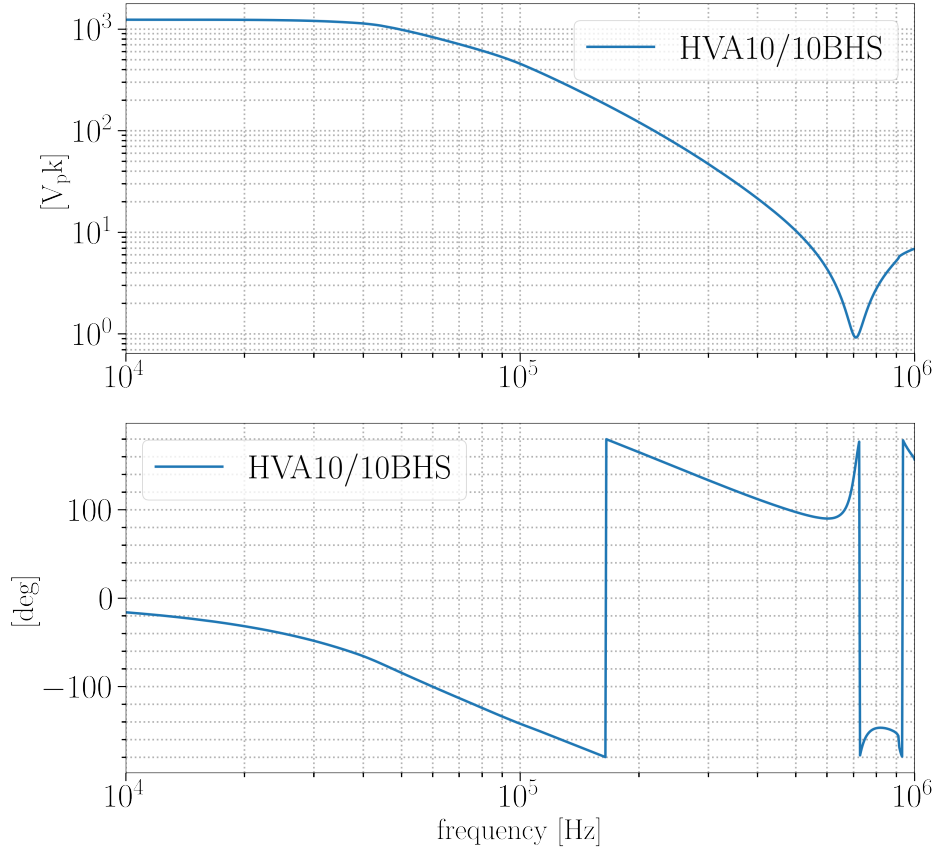


Figure 3.5: TREK 10/10B-HS HVA frequency dependent measurement. Using Poisson calculator to estimate field strength within coating. (Just HVA for now but will update. Also, assumes a flat response from coating within this studied region (is this a good assumption or could I do better? (dielectric frequency dependence))

3.3.3 Calibration

As discussed, we know that the error signal spectra provides us a voltage spectra that with the above information about the Plant/servo electronics, allows us to $\text{VFSSOUT}_{\text{rms}}/\sqrt{\text{Hz}} \rightarrow m_{\text{rms}}/\sqrt{\text{Hz}}$

$$\Delta L = \text{source} * \alpha(f)A(f) * \frac{1 + \text{OLG}(f)}{\text{OLG}(f)} * \frac{L_{\text{cav}}}{f_{\text{laser}}}$$

3.3.4 Noise Floor

Various noise contributions that add up to measured noise floor

Shot noise

Look at the derived shot noise estimate in the appendix V in the Black paper [18]

Laser frequency noise

- Measure with initial LIGO PMC?
- There is also a spectra in the Mephisto laser spec sheets

Residual gas noise

Mount noise (3D printed mount mechanical noise)

3.3.5 Drive coupling

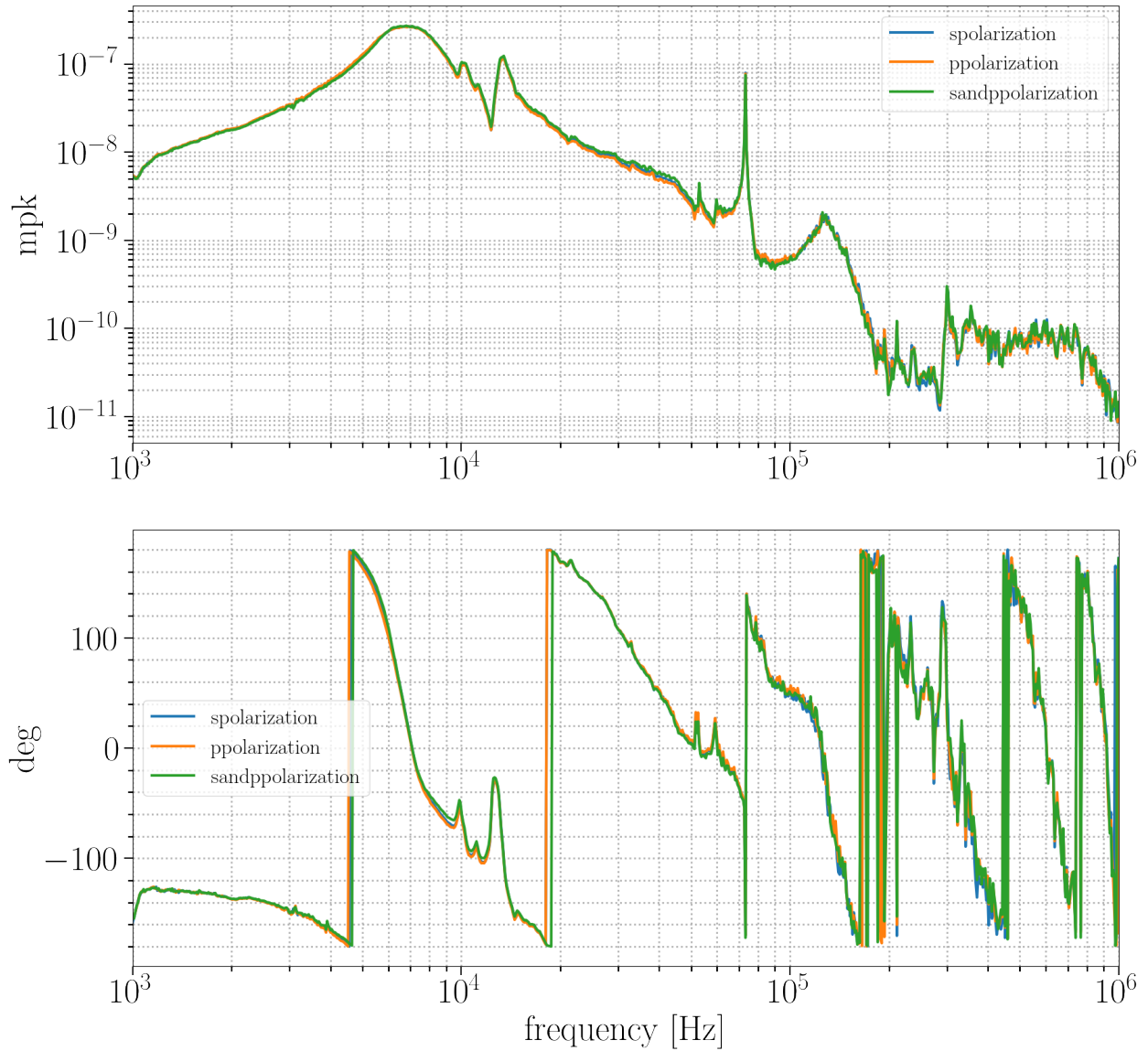


Figure 3.6: Figure that will include the displacement noise floor, (pockels estimate)*(poisson calculator estimate)*(HVA drive frequency dependence), and the drive coupled measurement
figure size needs to be increased

Opto-mechanical coupling

Sample and mount mechanical mode excitations. Seen with both AlGaAs and a HR coating from an AtFilm (IBS coating)

- **Vibration of plates (Leissa)** [19] Computing frequencies and order of magnitude
- **Steve's COMSOL model results**

Proposed alternative measurement schema

Chapter 4

Conclusion

Chapter 5

Appendix

5.1 The Equipartition theorem and the Fluctuation dissipation theorem

5.2 Crystal classification, point groups, and Bravais lattices

Crystal classification	Point groups		Bravais lattices
	Hermann-Mauguin	Schoenflies	
Triclinic	1 $\bar{1}$	C_1 C_i	P
Monoclinic	2 m $2/m$	C_2 C_s C_{2h}	P, C
Orthorombic	222 $mm2$ mmm	D_2 C_{2v} D_{2h}	P, C, I, F
Tetragonal	4 $\bar{4}$ $4/m$ 422 $4mm$ $\bar{4}2m$ $4/mmm$	C_4 S_4 C_{4h} D_4 C_{4v} D_{2d} D_{4h}	P, I
Trigonal	3 $\bar{3}$ 32 $3m$ $\bar{3}m$	C_3 C_{3i} D_3 C_{3v} D_{3d}	R
Hexagonal	6 $\bar{6}$ $6/m$ 622 $6mm$ $\bar{6}m2$ $6/mmm$	C_6 C_{3h} C_{6h} D_6 C_{6v} D_{3h} D_{6h}	P
Cubic	23 $m\bar{3}$ 432 $\bar{4}3m$ $m\bar{3}m$	T T_h O T_d O_h	P, I, F

Crystal Class → geometric analogy

Point groups

Bravais lattices

Space groups

5.3 Calibration

The frequency response measurement shown in (?) records the following transfer function in dB of the following:

$$\alpha(f) = \frac{CH2(f)}{Source} \quad (5.1)$$

Channel

We also know that the error signal spectra of the loop is probed by $CH2(f)$:

$$CH2(f) = \frac{S(f) * signal_V}{(1 - OLG(f))} \quad (5.2)$$

Where $signal_V$ is the uncalibrated voltage output from the mixer, $S(f)$ is the FSS transfer function, and $OLG(f)$ is the open loop gain of the PDH system.

And we know $OLG(f) = S(f) * A(f)$ so :

$$signal_m = CH2(f) * A(f) \frac{1 - OLG(f)}{OLG(f)} \frac{L_{cav}}{f_{laser}} \quad (5.3)$$

Where $A * (f)$ is the high voltage amplifier response with the Mephisto 2220 laser PZT response. L_{cav} is the sample cavity length, f_{laser} is the laser frequency. $(signal_m)$ is the effective cavity length change from the Pockels effect.

Substitute (1) into (4):

$$signal_m = Source * \alpha(f) * A(f) \frac{1 - OLG(f)}{OLG(f)} \frac{L_{cav}}{f_{laser}} \quad (5.4)$$

Measured : Source, $\alpha(f)$, $OLG(f)$, $A(f)$ and L_{cav}

5.4 Laplace calculator / code

5.5 MACOR assembly

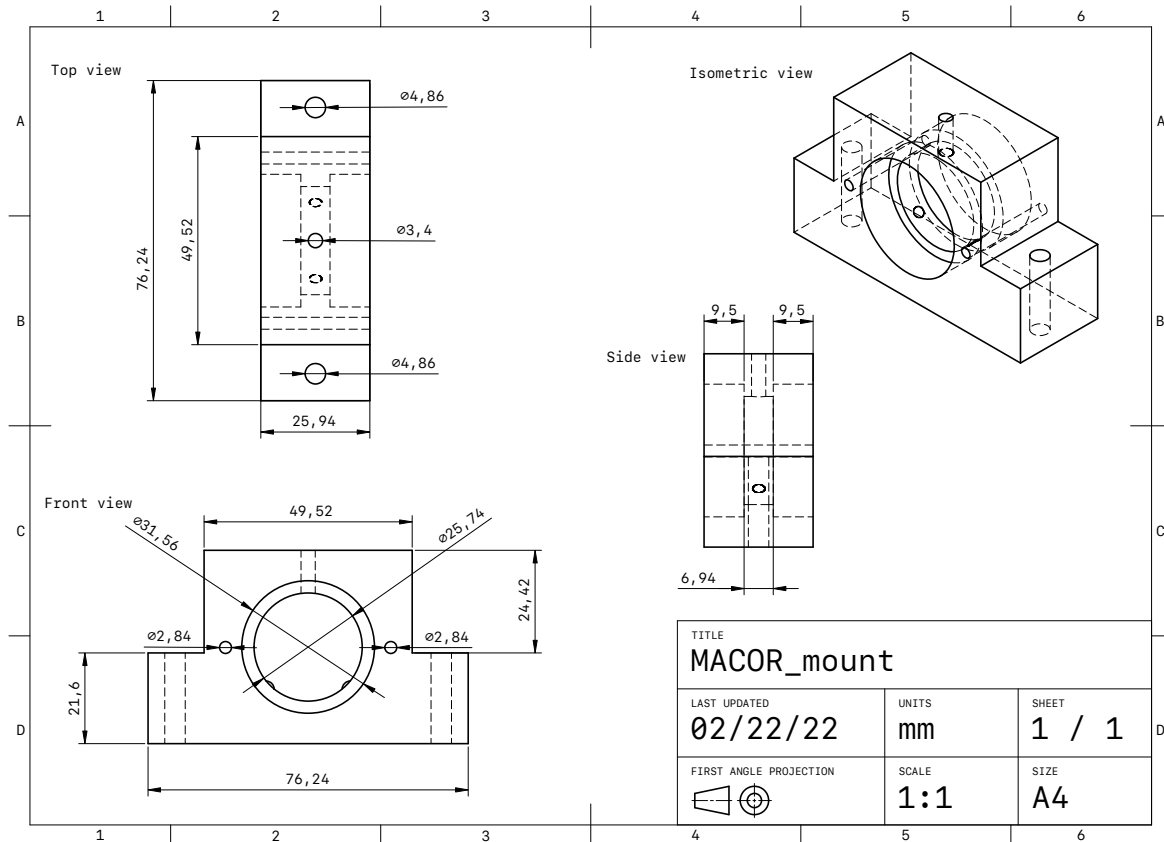
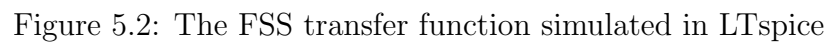


Figure 5.1: MACOR mount design constructed in Shapr3D

First angle projection is used in Europe. In America, third angle projection is used, and I recommend to use it.



References

- [1] T. Vo, *Adaptive Mode Matching in Advanced LIGO and beyond*. PhD thesis, Syracuse NY, 2019.
- [2] G. D. Cole, W. Zhang, M. J. Martin, J. Ye, and M. Aspelmeyer, “Tenfold reduction of brownian noise in high-reflectivity optical coatings,” *Nature Photonics*, vol. 7, no. 8, pp. 644–650, 2013.
- [3] M. Abernathy, “Noise in crystalline coatings,” Tech. Rep. G1401060-v1, LIGO Scientific Collaboration, August 2014.
- [4] R. B. F. H. M. . R. A. V.P.L.S., “Xxvii. a brief account of microscopical observations made in the months of june, july and august 1827, on the particles contained in the pollen of plants; and on the general existence of active molecules in organic and inorganic bodies,” *The Philosophical Magazine*, vol. 4, no. 21, pp. 161–173, 1828.
- [5] H. B. Callen and T. A. Welton, “Irreversibility and generalized noise,” *Phys. Rev.*, vol. 83, pp. 34–40, Jul 1951.
- [6] C. Zener, *Elasticity and Anelasticity of Metals*. University of Chicago Press, 1948.
- [7] Y. Levin, “Internal thermal noise in the ligo test masses: A direct approach,” *Physical Review D*, vol. 57, p. 659–663, Jan 1998.
- [8] T. Hong, H. Yang, E. K. Gustafson, R. X. Adhikari, and Y. Chen, “Brownian thermal noise in multilayer coated mirrors,” *Physical Review D*, vol. 87, Apr 2013.
- [9] G. M. Harry, H. Armandula, E. Black, D. R. M. Crooks, G. Cagnoli, J. Hough, P. Murray, S. Reid, S. Rowan, P. Sneddon, M. M. Fejer, R. Route, and S. D. Penn, “Thermal noise from optical coatings in gravitational wave detectors,” *Appl. Opt.*, vol. 45, pp. 1569–1574, Mar 2006.
- [10] J. F. Nye, *Physical properties of crystals (Their representation by tensors and matrices)*. Oxford University Press, 1985.

- [11] I. U. of Crystallography, *International Tables for Crystallography, Volume A1: Symmetry relations between space groups*. International Tables for Crystallography, Dordrecht, Boston, London: Kluwer Academic Publishers, 2nd online edition ed., 2011.
- [12] D. Sands, *Introduction to Crystallography*. Dover Books on Chemistry Series, Dover Publications, 1993.
- [13] A. Yariv, *Quantum Electronics (3rd. ed)*. John Wiley & Sons, 1989.
- [14] M. F. Edgard Bonilla, “Optical phase perturbations on the reflected wave of a dielectric mirror. application to the electro-optic effect in algaas coatings,” Tech. Rep. T1800528-v1, LIGO Scientific Collaboration, December 2018.
- [15] S. W. Ballmer, “Photothermal transfer function of dielectric mirrors for precision measurements,” *Physical Review D*, vol. 91, Jan 2015.
- [16] G. Mansell, “Electric field meter not coherent with darm (lho elog 56416).” <https://alog.ligo-wa.caltech.edu/aLOG/index.php?callRep=56416>.
- [17] Corning, *MACOR (Machinable glass ceramic for industrial applications)*, 2012. Available at <https://www.corning.com/media/worldwide/csm/documents/71759a443535431395eb34ehead091cb.pdf>.
- [18] E. D. Black, “An introduction to pound–drever–hall laser frequency stabilization,” *American Journal of Physics*, vol. 69, no. 1, pp. 79–87, 2001.
- [19] A. W. Leissa, *Vibration of Plates*. National Aeronautics and Space Administration Special Publication (SP), 1969.